Past Ocean surface density from planktonic foraminifera calcite $\delta^{18}O$

Thibaut Caley[1], Niclas Rieger[2,3], Martin Werner[4], Claire Waelbroeck[5], Héloise Barathieu[1], Tamara Happé[6], Didier M. Roche[7,8]

1) Univ. Bordeaux, CNRS, Bordeaux INP, EPOC, UMR 5805, 33600 Pessac, France

2) Institut de Ciències del Mar (ICM) - CSIC, Pg. Marítim de la Barceloneta 37, Barcelona, Spain

3) Centre de Recerca Matemàtica (CRM), Departament de Física, Bellaterra, Spain

4) Alfred Wegener Institute Helmholtz Centre for Polar and Marine Research, Bremerhaven, Germany

5) LOCEAN-IPSL, CNRS, Sorbonne Université, Paris, France

6) Institute for Environmental Studies, Vrije Universiteit Amsterdam, Amsterdam, The Netherlands

7) Laboratoire des Sciences du Climat et de l'Environnement, LSCE/IPSL, CEA-CNRS-UVSQ, Université Paris-Saclay, 91191 Gif-sur-Yvette, France

8) Earth and Climate Cluster, Faculty of Earth and Life Sciences, Vrije Universiteit Amsterdam, Amsterdam, the Netherlands

Correspondence to: Thibaut Caley (thibaut.caley@u-bordeaux.fr)

Abstract

Density of seawater is a critical property that controls ocean dynamics. Previous works suggest the use of the $\delta^{18}O$ calcite of foraminifera as a potential proxy for paleodensity. However, potential quantitative reconstructions were limited to the tropical and subtropical surface ocean and without an explicit estimate of the uncertainty in calibration model parameters. We developed the use of the $\delta^{18}Oc$ of planktonic foraminifera as a surface paleodensity proxy using Bayesian regression models calibrated to annual surface density. Predictive performance of the models improves when we account for inter-species specific differences.

We investigate the additional uncertainties that could be introduced by potential evolution of the $\delta^{18}Oc$-density relationship with time (from the last glacial maximum (LGM) to the preindustrial (PI)) through the combination of past isotope enabled climate model simulations and a foraminiferal growth module. We demonstrate that additional uncertainties are weak globally, except for the Nordic Seas region.

We applied our Bayesian regression model to LGM and Late Holocene (LH) $\delta^{18}Oc$ foraminifera databases to reconstruct annual surface density during these periods. We observe stronger LGM density value changes at low latitudes compared to mid latitudes. These results will be used to evaluate numerical climate models in their ability to simulate ocean surface density during the extreme climatic period of the LGM.

The new calibration has great potential to reconstruct the past temporal evolution of ocean surface density over the Quaternary. Under climates outside the Quaternary period and in ocean basins characterized by anti-estuary circulation, like the current Mediterranean Sea and Red Sea, our calibration could provide density estimates with larger uncertainty, a point that requires further investigations.

1. Introduction

Temperature and salinity control the density of seawater and therefore the ocean dynamics too. Reconstruction of past ocean surface temperature with reasonable uncertainties is possible (MARGO, 2009; Tierney et al., 2020b) but reconstructions of past surface salinity remain very challenging in paleoceanography. When the current uncertainties on past temperature and salinity reconstructions are cumulated, it becomes unreasonable to combine these two parameters in order to quantify past ocean density and dynamics (Schmidt, 1999).

Rather than using the combination of temperature and salinity, previous works suggest the use of the $\delta^{18}O$ of foraminiferal calcite as a potential proxy for paleodensity (Lynch-Stieglitz et al., 1999; Billups and Schrag, 2000, LeGrande et al., 2004; Lynch-Stieglitz et al., 2007). The oxygen isotopic composition of foraminifera calcite is controlled by 1) the temperature dependence of the equilibrium fractionation during calcite precipitation and 2) the isotopic composition of seawater in which the shell grows (Urey, 1947; Shackleton, 1974). Except in areas of sea ice formation or melt, the isotopic composition of seawater ($\delta^{18}O_{sw}$) is regionally related to salinity, since they are affected by processes such as evaporation, precipitation, and the water masses advection and mixing (Craig and Gordon, 1965). Therefore, both temperature and $\delta^{18}O_{sw}$ changes that affect the foraminifera $\delta^{18}O$ calcite ($\delta^{18}Oc$) signal are also the processes that ultimately define the seawater density in which the foraminifera calcifies (Lynch-Stieglitz, 1999; Billups and Schrag, 2000).

In addition to temperature and $\delta^{18}Osw$, the shell $\delta^{18}Oc$ signal can also be potentially influenced by biological processes, such as: 1) photosynthesis in algal symbionts (Duplessy et al., 1970; Ravelo and Fairbanks, 1992; Spero and Lea, 1993; Spero et al., 1997) and biases due to the formation of gametogenic or ontogenetic calcite (Williams et al., 1979; Spero and Lea, 1996; Hamilton et al., 2008), 2) changes in pH and carbonate ion concentration $[CO^{2-}_3]$ (Spero et al., 1997; Bijma et al., 1999; Zeebe, 1999), 3) dissolution and recrystallization for shells deposited in bottom waters undersaturated in $[CO^{2-}_3]$ (Schrag et al., 1995), and 4) bioturbation (Waelbroeck et al., 2005). The four processes mentioned above have not been clearly demonstrated. In addition, the carbonate ion effect has been shown to have no detectable influence (Köhler and Mulitza, 2024) and core top data have been selected to limit the bioturbation effect (Waelbroeck et al., 2005). Therefore, we do not account for these processes. Transport of foraminifera shells by currents is another process that could lead to discrepancies between recorded $\delta^{18}Oc$ and calculated $\delta^{18}Oc$ or hydrographic data. However, this effect is likely minimal because the ambient water mass is transported together with the shells. Later in this study (Sect. 3.1.2), we confirm that planktonic foraminifera $\delta^{18}Oc$ is mainly related to the surface ocean density, growth season and habitat depth, with weak additional influence from biological processes.

Previously, Billups and Schrag (2000) used $\delta^{18}Oc$ from the mixed layer planktonic foraminifera (*Globigerinoides ruber* and *Trilobatus sacculifer*) as a proxy of surface water density. They limited their study to the tropical and subtropical surface ocean.

109 In this study we investigate the use of planktonic foraminifera δ¹⁸Oc as a surface
110 paleodensity proxy for the whole ocean, from low to high latitudes, using various
111 foraminifera species: *Globigerinoides ruber* (*G. ruber*), *Trilobatus sacculifer* (*T. sacculifer*),
112 *Globigerina bulloides* (*G. bulloides*), *Neogloboquadrina incompta* (*N. incompta*), and
113 *Neogloboquadrina pachyderma* (*N. pachyderma*). Compared to Billups and Schrag (2000), we
114 use extended late Holocene (LH) and last glacial maximum (LGM) δ¹⁸Oc databases
115 (Malevitch et al., 2019; Caley et al., 2014, Waelbroeck et al., 2014; Tierney et al., 2020b). We
116 develop mean annual surface density calibration models using a Bayesian approach. We also
117 use numerical climate simulations obtained with isotope enabled climate models
118 (iLOVECLIM and ECHAM5/MPI-OM) and a foraminiferal growth module (FAME) (Roche et al.,
119 2018) to investigate the specific seasonal dynamic and depth habitat preference of
120 foraminifera (Roche et al., 2018; Schiebel and Hemleben 2018). We discuss the applicability
121 and validity of the foraminifera δ¹⁸Oc to the past quantification of surface ocean density. We
122 then reconstruct past surface density changes during the LGM.

123

124 2. Methods
125 2.1 Planktonic foraminifera δ¹⁸O databases

126 We compiled global foraminifera oxygen isotopic datasets from published LH and LGM
127 measurements to allow reconstruction of past density. We used core-top and LH records of
128 planktonic foraminifera δ¹⁸Oc from Malevich et al. 2019 dataset that include records from
129 the Multiproxy Approach for the Reconstruction of the Glacial Ocean (MARGO) (Waelbroeck
130 et al., 2005) with additional sources. This dataset consists of 2,636 observations with 1,002
131 for *G. ruber*, 635 for *G. bulloides*, 442 for *T. sacculifer*, 132 for *N. incompta* and 425 for *N.
132 pachyderma* (Malevich et al., 2019). Similarly to Malevich et al. 2019, we gridded the core-
133 top data to reduce the impact of spatial clustering by averaging samples for each species to
134 the nearest 1°X 1° grid point. So doing, we obtained a total of 1,415 grid points.

135 For the LGM time period, records derived in part from the MARGO collection (Waelbroeck et
136 al., 2014), with additional data from Caley et al., 2014, Tierney et al., 2020b, and from more
137 recent studies (34 measurements). The final dataset consists of 474 observations.
138 Chronostratigraphic quality for the LGM and LH is consistent between all the published
139 databases, the additional observations and use the same MARGO definition (MARGO, 2009).

140 2.2 Ocean dataset

141 In order to establish and test our calibrations between foraminifera δ¹⁸Oc and observed
142 surface density, we used different ocean datasets. We used the Multi Observation Global
143 Ocean Sea Surface density product for our core-top and Late Holocene calibration models
144 (Droghei et al., 2016; 2018). This means that we calibrated Late Holocene core-top samples
145 against observed density fields influenced by anthropogenic climate change, an issue that
146 affects all core-top calibrations. To test the residual of our models against sea surface
147 temperature and salinity (SST and SSS respectively) we used WOA18 products (Locarnini et
148 al., 2018; Zweng et al., 2018).

149

2.3 Bayesian calibration models and evaluation

151

Following the general approach of Malevich et al. (2019), we use Bayesian regressions to model the relationship between the calcite oxygen isotopic composition of planktonic foraminifera, $\delta^{18}Oc$ (‰ VPDB), and annual mean surface density, ρ (kg/m^3 relative to the water density of 1000 kg/m^3). By explicitly estimating uncertainty in the calibration model parameters, each model produces a full posterior predictive distribution for the predictant ρ. We implement three Bayesian models—two pooling models with first- and second-degree polynomials, and a hierarchical first-degree polynomial model—using Markov chain Monte Carlo (MCMC) methods (see Kruschke, 2014; McElreath, 2018 for review).

2.3.1 Three Bayesian calibration models

1. **First-Degree Polynomial (Pooled), poly1_pool:**
   A simple linear regression is fit to all foraminifera species combined:
   $$\rho \sim N(\mu, \sigma^2), \quad \mu = \beta_0 + \beta_1 \delta^{18}O_c.$$
   Weakly informative data-adaptiv normal hyperpriors are used for β_0 and β_1, and an exponential prior for the noise term sigma. This pooled model assumes a common relationship across all foraminifera species (see Appendix).

2. **Second-Degree Polynomial (Pooled), poly2_pool:**
   Motivated by empirical evidence (e.g., Billups and Schrag (2000)), the second model incorporates a quadratic term:
   $$\rho \sim N(\mu, \sigma^2), \quad \mu = \beta_0 + \beta_1 \delta^{18}O_c + \beta_2 (\delta^{18}O_c)^2.$$
   Again, we apply weakly informative normal priors for the β_i parameters, ensuring flexibility while constraining the plausible range based on the observed data.

3. **First-Degree Polynomial (Hierarchical), poly1_hier:**
   The third model recognizes that species-specific differences in calcification, depth, seasonality and vital effects can affect $\delta^{18}O_c$ (Malevich et al., 2019). Hence, we use a hierarchical structure:
   $$\rho \sim N(\mu_s, \sigma_s{}^2), \quad \mu_s = \beta_{s,0} + \beta_{s,1} \delta^{18}O_c.$$
   where each species s has its own intercept ($\beta_{s,0}$) and slope ($\beta_{s,1}$). These species-level parameters are drawn from common hyperdistributions ν_i and κ_i (Appendix A), ensuring partial pooling of information across species.

2.3.2 Model fitting and evaluation

182

All models were fitted with six independent MCMC chains of 4000 iterations each, discarding the first 2000 as burn-in. We used rank-normalized $\hat{R}$ (Vehtari et al. 2021) to assess convergence, finding all values below 1.05. Prior and posterior predictive checks confirmed the adequacy of the models. To compare predictive performance, we computed the expected log pointwise predictive density (ELPD) via Pareto-smoothed importance sampling leave-one-out cross-validation (LOO) (Vehtari et al., 2017), which provides a principled basis for selecting the model that best characterizes the relationship between $\delta^{18}Oc$ and ρ. The

190 ELPD measures the expected predictive accuracy of a Bayesian model. It is defined as the
191 sum over all data points of the expected log posterior predictive density (Gelman et al.,
192 2014). In our case, a higher ELPD means the model makes sharper and more accurate
193 density predictions.

194

195   2.4 Isotope enabled numerical climate models

196 2.4.1 The iLOVECLIM model

197 The iLOVECLIM (version 1.1.3) earth system model of intermediate-complexity is a derivative
198 of the LOVECLIM-1.2 climate model extensively described in Goosse et al. (2010). From the
199 original model, we retain the atmospheric (ECBilt, resolution of 5.6° in latitude and
200 longitude), oceanic (CLIO, 3x3° horizontal resolution, 20 vertical layers and a free surface),
201 vegetation (VECODE) and land surface (LBM) components and develop a complete,
202 conservative, water isotope cycle through all cited components. A detailed description of the
203 method used to compute the oxygen isotopes in iLOVECLIM can be found in Roche (2013)
204 and the validation of model results can be found in Roche and Caley (2013), Caley and Roche
205 (2013) and Extier et al., 2024.

206 We use the boundary conditions defined in/by the PMIP2 protocol to simulate the annual
207 LGM climate (Caley et al., 2014). Details about the model simulations (LGM and pre-
208 industrial (PI)) and validation of results for oxygen stable isotopes and temperature can be
209 found in Caley et al. 2014.

210 2.4.2 The ECHAM5/MPI-OM model

211 We also use the ECHAM5/MPI-OM coupled General Circulation Model (GCM), also
212 previously named community Earth system model COSMOS. It is a fully coupled ocean–
213 atmosphere–sea ice– land surface model (Jungclaus et al., 2006) with stable water isotope
214 diagnostics in all relevant model components. Mass, energy, and momentum fluxes, as well
215 as the related isotope masses of $H_2^{18}O$ and HDO, are exchanged between the atmosphere
216 and ocean once per day. Further details about the model can be found in Werner et al.,
217 2016.

218 We used monthly outputs of the two simulations performed for the PI and for the LGM
219 climate as described and evaluated for oxygen stable isotopes in Werner et al., 2016.

220

221   2.5 The FAME module

222 Foraminifera as Modelled Entities (FAME; Roche et al., 2018) is a foraminiferal growth
223 module that tackles the dynamic seasonal and depth habitat of planktonic foraminifera. The
224 module predicts the presence or absence of commonly used planktonic foraminifera and
225 their $\delta^{18}O$ values. It uses a very limited number of parameters, almost all derived from
226 culture experiments (Lombard et al., 2009).

227

228 ## 3. Results and discussion

229 ### 3.1 Ocean surface density from planktonic foraminifera calcite $\delta^{18}O$

230 The three Bayesian calibration models reasonably replicate core top data spread when we
231 predict surface density (Fig. 1).

232
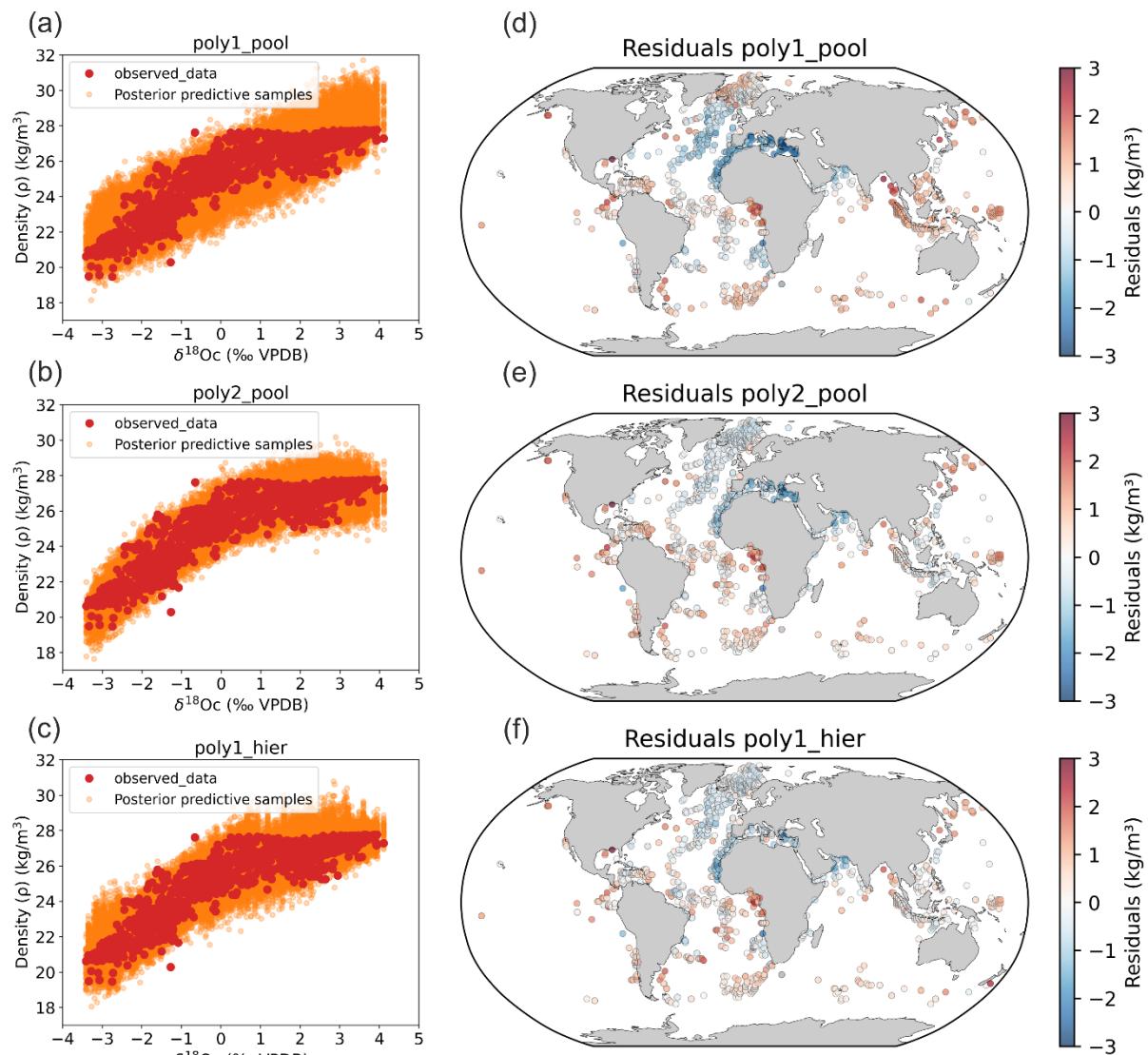
233

234 Figure 1: Bayesian calibration models for late Holocene core-top samples against observed
235 density. (a), (b) and (c) The three Bayesian regression models between foraminifera $\delta^{18}Oc$
236 and annual surface density and (d), (e) and (f) associated density residuals (predicted -
237 observed).

238 Compared to the Billups and Schrag (2000) study which was restricted to the 21-26 density
239 range in tropical and subtropical regions, our models provide estimates of the density
240 changes over the whole density range from 19 to 28 (Fig. 1). In our new calibrations, we also
241 explicitly estimate the uncertainty in calibration model parameters (Fig. 1) using a Bayesian
242 approach to calculate robust confidence intervals.

253   3.1.1 Model comparison and residuals

254 Looking at the density residual (predicted - observed) for the three models, the first model
255 (linear pools) has the highest values of residual and the third model (hierarchical design)
256 performs best (Fig. 1). The second model performs clearly better than the first one but less
257 than the hierarchical design. This is supported by model evaluation using log pointwise
258 predictive density (ELPD) (Vehtari et al., 2017) (Fig. 2). Predictive performance of the model
259 improves when we account for species-specific differences and species-specific prediction
260 uncertainty (sigma) in surface density predictions vary between foraminifera species (Fig. 2).
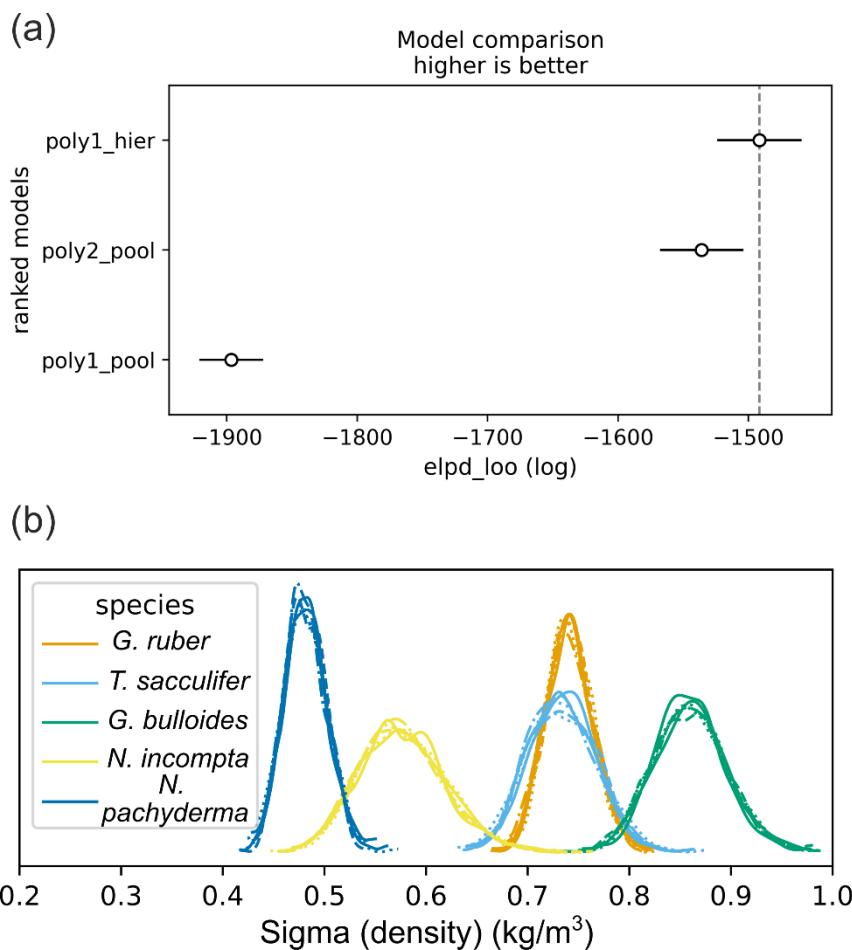
Figure 2: Model comparison and prediction uncertainty across species. (a) Expected log pointwise predictive density (ELPD) for the three models; higher values indicate better predictive performance. (b) Posterior distributions of the prediction-error parameter (sigma density) from the hierarchical model for each foraminifera species (six MCMC chains shown). Among these, *N. pachyderma* exhibits the lowest uncertainty, while *G. bulloides* shows the highest.

We still observe residuals with the hierarchical model (Fig. 1), so we checked their relation to SST and SSS (Fig. 3). The residuals of the pooled linear annual calibration model exhibit a relationship with SST and a linear relationship with SSS with a relatively high correlation ($R^2 = 0.55$, p-value <0.05). In contrast, the residuals of the hierarchical annual calibration model show no correlation to SST ($R^2 = 0$, p-value <0.05) and only a very weak correlation with SSS ($R^2 = 0.21$, p-value <0.05). This suggests that factors other than SST and SSS influence the remaining residual structures, and some may be indirectly associated with SSS gradients. Indeed, ecological factors (e.g. seasonality and habitat depth) and secondary environmental parameters (e.g. nutrients and light penetration) may also contribute. This is supported by the fact that the residual of individual species (Fig. 3) show various significant relations (p-value <0.05) with SSS, with R^2 values of 0.17 for *G. ruber*, 0.12 for *T. sacculifer*, 0.54 for *G. bulloides*, 0.15 for *N. incompta*, and 0.32 for *N. pachyderma*. For example, negative residuals are observed in the Benguela, Canary, Peru and North Arabian regions (Fig. 1). All these coastal areas correspond to upwelling systems and previous work already suggested that foraminifera species could have a preference for nutrient-rich waters with high turbidity. This is particularly true for the seasonal specie *G. bulloides* (Peeters et al., 2002; Gibson et al., 2016). The $\delta^{18}Oc$ may therefore be biased toward colder temperatures even when accounting for seasonality and species-specific sensitivity (Malevich et al., 2019). This could explain why all three models yield lower densities than the observed annual mean densities in the upwelling zones. The negative density residuals in these upwelling regions may reflect this habitat preference (Fig. 1).
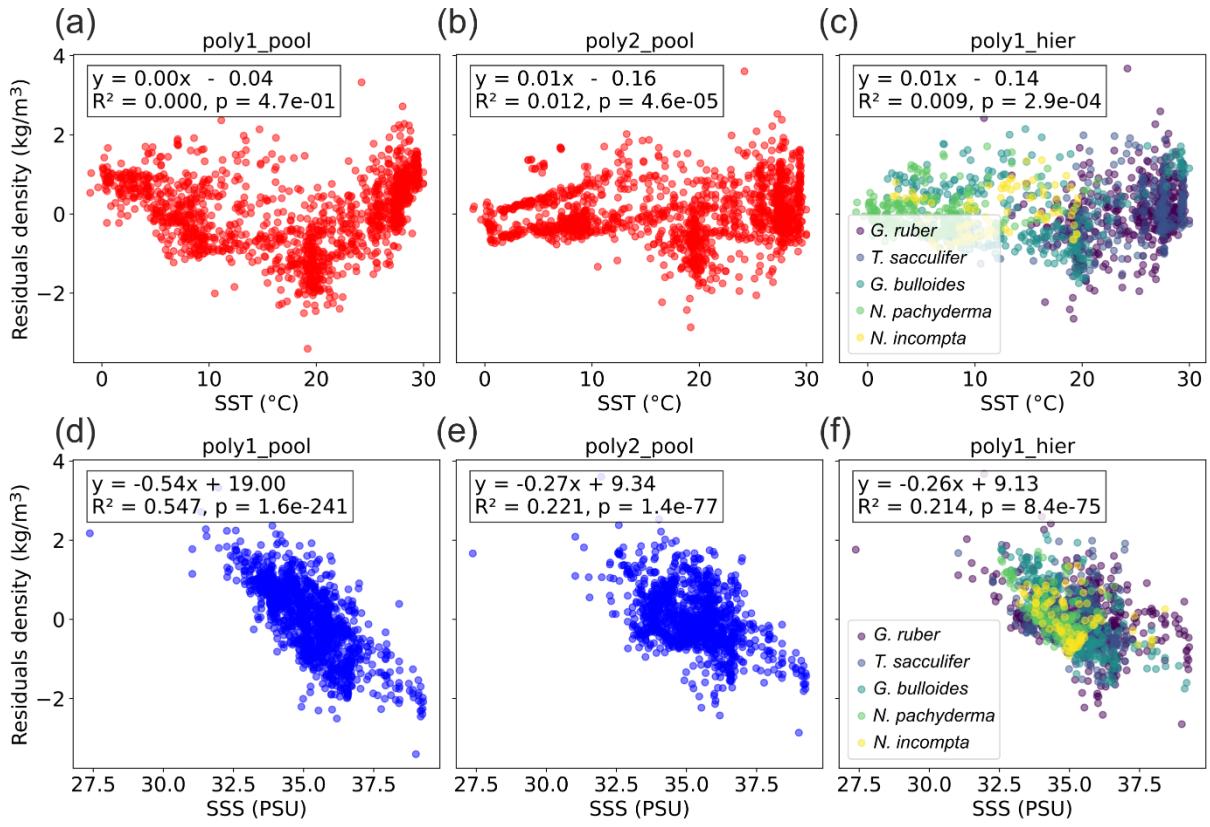
Figure 3: Relation between density residuals (predicted - observed) and (a), (b) and (c) for SST and (d), (e) and (f) for SSS (WOA18 products, Locarnini et al., 2018; Zweng et al., 2018) for the three Bayesian regression models. R^2 and p-values are indicated.

Strong negative residuals are also observed in the eastern part of the Mediterranean Sea. Malevich et al. 2019 reported reduced performance of their hierarchical seasonal calibration model for $\delta^{18}Oc$ and SST in this region and attributed it to the unusual behavior of *G. ruber,* potentially linked to depth-habitat migration. But estimation of seasonality for this region could also be problematic and play a role as highlighted in the study of Ayache et al. 2024. Alternatively, biases in Mediterranean net freshwater fluxes and thermohaline circulation could affect late Holocene $\delta^{18}Oc$ values (Ayache et al., 2014). Future modelling developments, such as the use of high-resolution regional model in combination with the FAME module, could help to better understand the relation between $\delta^{18}Oc$, density, temperature and $\delta^{18}Osw$ during past climate changes in the Mediterranean Sea.

We also observe high positive residual values in the Equatorial and South Atlantic Ocean, in particular on the equatorial African margin and to a lesser degree in the Equatorial East Pacific Ocean. As discussed later (Sect. 3.1.2), these positive density residuals could be related to ecological factors such as seasonality.

It is possible to take into account seasonality based on an estimation of foraminiferal seasonal abundance (Malevich et al. 2019), or using the FAME module. This module predicts the mean $\delta^{18}Oc$ of a foraminifera sample constituted of a number of individuals by weighting in space (depth in the water column) and time (months) the oceanic conditions by the growth rate of each individual.

329 We decided to not directly develop seasonal calibration models for several reasons. First, we
330 want to predict annual surface density to be able to compare and evaluate numerical
331 climate models against annual surface density. Second, including seasonal signals in
332 foraminifera in our Bayesian models using sediment trap data (Malevich et al. 2019) or
333 seasonality and habitat depth using FAME (that uses the temperature dependence of growth
334 derived from culture experiments (Lombard et al., 2009)) would be a simplification that does
335 not consider factors such as light and nutrient availability. Third, even if it could potentially
336 improve the models for the present day calibration, although a hierarchical seasonal model
337 does not necessary show an increase in validation performance compared to the hierarchical
338 annual model (Malevich et al., 2019), this approach assumes that seasonality or habitat
339 depth would not change during past periods. Results using FAME demonstrate that
340 seasonality or habitat depth change during past periods (Roche et al., 2018). Therefore,
341 changes in seasonality and habitat depth could introduce additional uncertainties when
342 using a seasonal calibration model to predict past seasonal surface density. One possibility
343 would be to use simulation results for past periods to force the FAME module and create
344 past Bayesian calibration models between $\delta^{18}Oc$ and surface density that would take into
345 account ecological changes. However this would not be independent of climate models and
346 would lead to circular reasoning if the purpose is to use reconstructed density for
347 comparison and evaluation of past climate simulations.

348 We therefore adopt a different strategy. We use past isotope enable climate model
349 simulations for the pre-industrial (PI) and LGM periods to force the FAME module in order to
350 test within the "model world" if a PI Bayesian calibration (hierarchical design) between the
351 $\delta^{18}Oc$ and annual surface ocean density is stable with time and if the changes in foraminifera
352 growth season and habitat depth lead to additional uncertainties when applying a PI relation
353 to past annual predictions (LGM).

354

355 3.1.2 Testing the stability of the $\delta^{18}Oc$-density relation during past periods

356 Because the proposed approach to reconstruct ocean surface density uses the temperature
357 and $\delta^{18}Osw$ influence on the $\delta^{18}Oc$ signal, we investigated the potential evolution of the
358 $\delta^{18}Oc$-density relationship with time before applying this approach to past density
359 reconstructions. In particular, we investigated two questions: does the present day $\delta^{18}Osw$-
360 salinity relationship and its known past temporal evolution (Rohling, 2000, LeGrande and
361 Schmidt, 2011, Caley and Roche, 2015) significantly affect the density-$\delta^{18}Oc$ relation
362 evolution? Do ecological changes (foraminifera growth season and habitat depth)
363 significantly affect the density-$\delta^{18}Oc$ relation evolution?

364 We use numerical climate simulations (LGM and PI) of two isotope enabled numerical
365 climate models, iLOVECLIM and ECHAM5/MPI-OM, to address these questions. We calculate
366 the $\delta^{18}Oc$ signal based on the simulated $\delta^{18}Osw$ and ocean temperature for both PI and LGM
367 using the quadratic approximation of Kim and O'Neil (1997) given in Bemis et al. (1998). We
368 use the FAME module to predict the $\delta^{18}Oc$ values and account for foraminifera specific living
369 habitats in the water column and along the year as described in Roche et al. (2018). A

comparison of the simulated and observed core-top data δ¹⁸Oc (Fig. 4) shows high correlation (R^2 of 0.93 and 0.89 for ECHAM5/MPI-OM and iLOVECLIM respectively). The slightly higher correlation with ECHAM5/MPI-OM and associated lower root mean square error (RMSE) (Fig. 4) could be related to differences in climate models but also to the fact that in the chosen configuration iLOVECLIM generated only annual δ¹⁸Osw and ocean temperature hydrographic data contrary to ECHAM5/MPI-OM that produces monthly results. Therefore, the seasonality effect is only simulated by combining FAME and ECHAM5/MPI-OM whereas the habitat depth effect is simulated in both experiments.

We tested this hypothesis by using yearly ECHAM5/MPI-OM values to compute the δ¹⁸Oc and compared the results with those obtained with seasonal values (shown in Figure 4a) and better assess the effect of seasonality. Results indicate a slight decrease of the R^2 of 0.02 and a slight increase in RMSE of 0.06 when seasonality is not taken into account. These differences are significant according to paired t-tests. Therefore, seasonality partly explains the small difference between the results using ECHAM5/MPI-OM and iLOVECLIM. Lower resolution of iLOVECLIM or other missing/biased processes in this model could also contribute to this small difference.

Although climate models are not perfect, the observed high correlations demonstrate that 1) these numerical climate models can be used to address our questions regarding the stability of the δ¹⁸Oc-density relation during the past and 2) our hypothesis that planktonic foraminifera δ¹⁸Oc is mainly related to the surface ocean density, growth season and habitat depth, with weak additional influence by biological processes (Sect. 1.) is valid.
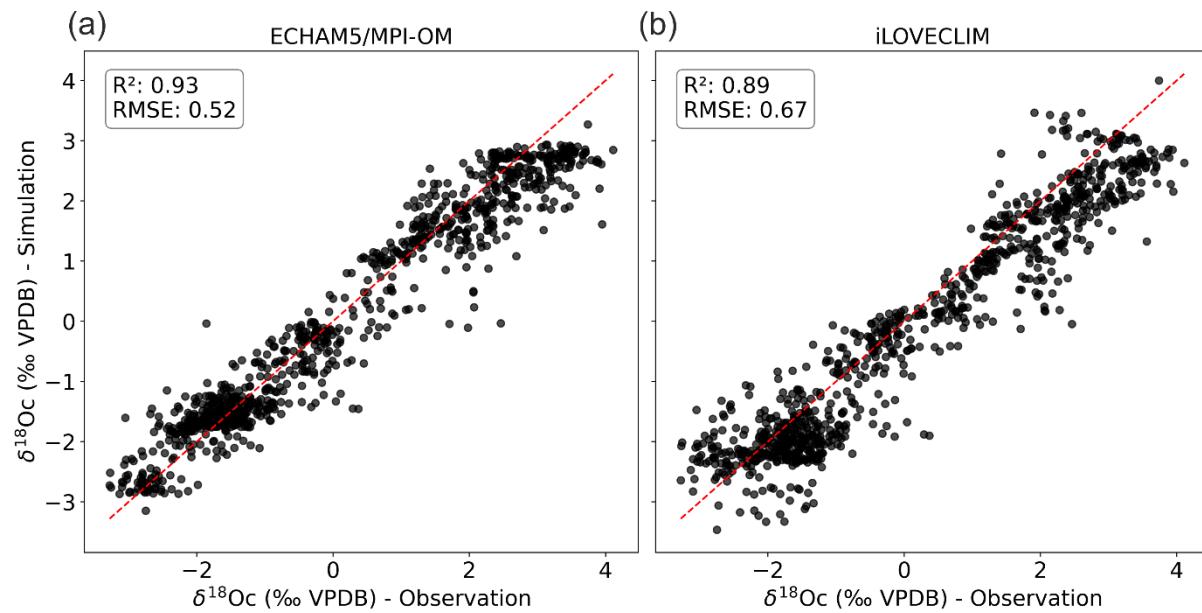
Figure 4: comparison between simulated PI foraminifera δ¹⁸Oc (FAME module forced with (a) ECHAM5/MPI-OM and (b) iLOVECLIM climate model hydrographic data) and observed LH core-top δ¹⁸Oc data. The 1:1 line is indicated.

We developed two PI Bayesian calibrations (hierarchical design) between the δ¹⁸Oc and annual surface ocean density based on FAME forced by ECHAM5/MPI-OM and iLOVECLIM hydrographic data (Fig. 5a). These Bayesian calibration models are comparable to the

407 poly1_hier Bayesian calibration model of Fig. 1. We then used the LGM simulations to force
408 FAME and produce δ^{18}Oc LGM values comparable to those that could be measured in a
409 marine sediment core (but in the model world). We can use these δ^{18}Oc LGM values and the
410 PI Bayesian calibrations to predict the ocean surface density at the LGM. We can then
411 compare the density reconstructed from the δ^{18}Oc values to the density simulated directly at
412 the LGM by ECHAM5/MPI-OM and iLOVECLIM. This furnish a test in the model world
413 regarding the stability of the δ^{18}Oc-density relation during the past.

414 Interestingly, the observed (Fig. 1) and simulated (Fig. 5b and e) density residuals (predicted
415 - observed) are overall in good agreement for both PI ECHAM5/MPI-OM and iLOVECLIM
416 experiments in terms of qualitative changes (positive or negative residuals) (Fig. 5b and e
417 and Fig. 1). Nonetheless, differences for some regions in terms of magnitude of the residual
418 values exist between ECHAM5/MPI-OM and iLOVECLIM experiments. We observe high
419 positive residuals in the Equatorial and South Atlantic Ocean in the ECHAM5/MPI-OM
420 experiment, in particular on the equatorial African margin and in the Equatorial East Pacific
421 Ocean. As discussed before (Sect. 3.1.1), these positive density residuals are also visible in
422 the observations (Fig. 1f). We attribute these high positive residuals in ECHAM5/MPI-OM
423 (Fig. 5b) that better fit the observations (Fig. 1f) to a seasonality effect because seasonality is
424 only taken into account in ECHAM5/MPI-OM experiment. Negative residuals previously
425 discussed in upwelling regions are visible in simulated residuals but with lower magnitude in
426 comparison to observations (Fig. 1f and 5b and e). This could be related to the fact that
427 upwellings are not well simulated in the two experiments or to the role of secondary
428 environmental parameters such as nutrients and light penetration.

429 We apply the PI annual Bayesian calibration to the simulated LGM δ^{18}Oc after a correction of
430 1.0‰ of LGM δ^{18}Osw values (value added at LGM for the ECHAM5/MPI-OM and iLOVECLIM
431 experiments, Caley et al., 2014, Werner et al., 2016) to account to a change of the global
432 oceanic δ^{18}Osw signal due to the increased LGM ice sheets. This yields a prediction of the
433 LGM surface ocean density that we can compare to the directly simulated LGM surface
434 density in both experiments. We calculate the density residual at the LGM (density
435 reconstructed from the δ^{18}Oc values - density simulated directly at the LGM). Finally, we
436 calculate the density residuals anomaly between LGM and PI as: density residuals at LGM -
437 density residuals at PI (Fig. 5c and f). This allows us to investigate the additional uncertainties
438 linked to the evolution of the density-δ^{18}Oc relation (Fig. 5c and f).

439
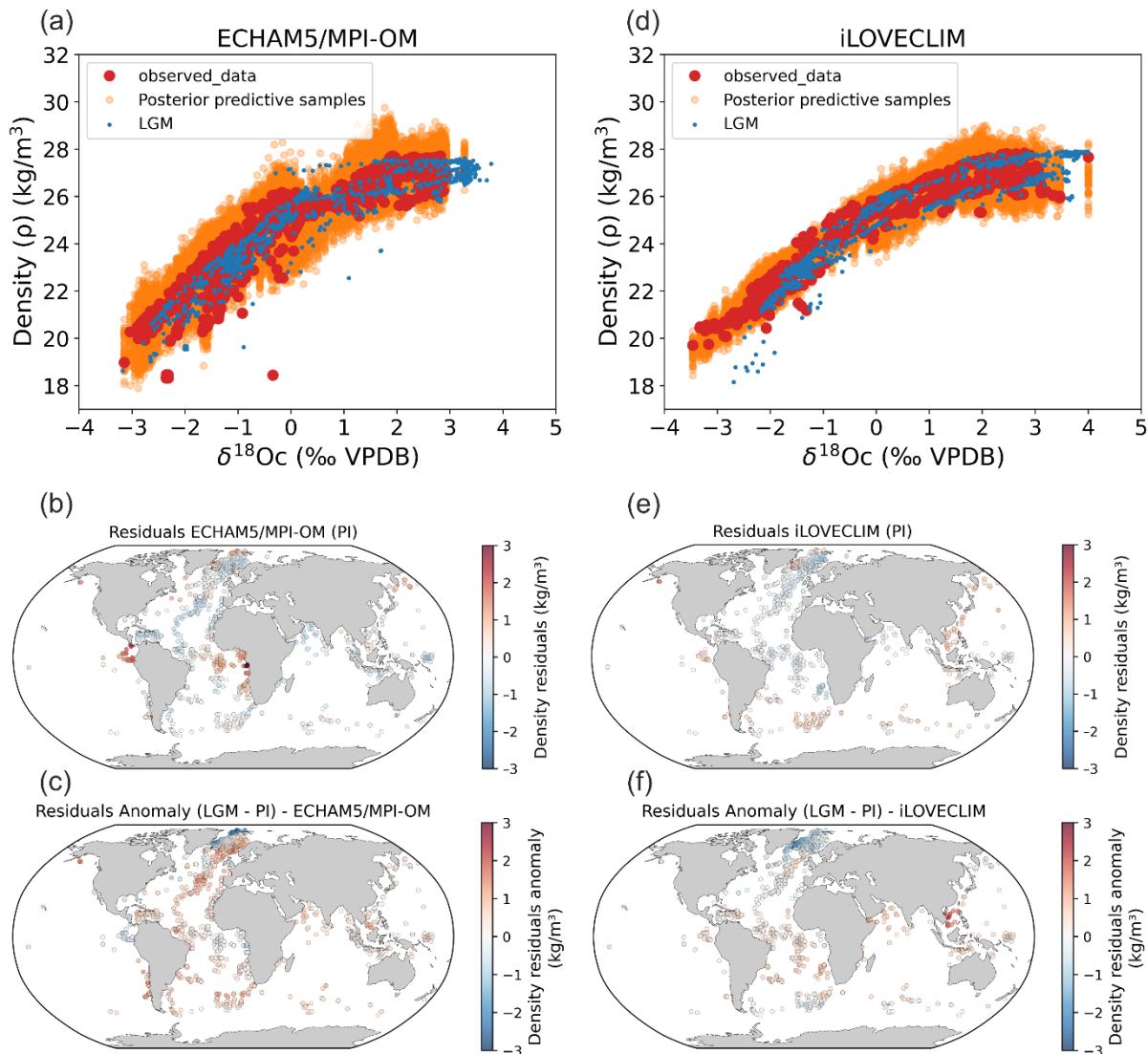
Figure 5: Stability of foraminifera δ^{18}Oc-density relations between PI and the LGM calculated with FAME and forced by global ECHAM5/MPI-OM (left panels, Werner et al., 2016) and iLOVECLIM (right panels, Caley et al., 2014) hydrographic data. (a) and (d) PI Bayesian regression models between foraminifera δ^{18}Oc and annual surface density. Data in the PI experiments have been selected at the same locations as observations (Fig. 1). Posterior predictive samples and the LGM δ^{18}Oc-density relation (LGM) are visible. (b) and (e) Density residuals (predicted - observed) for the PI experiments. (c) and (f) Density residuals anomaly between LGM and PI. Results for the Mediterranean Sea have been excluded because of its difficulty to be simulated and inconsistency between the two model simulations because of their different grid resolutions. Annual mean temperature and δ^{18}Osw were used for the iLOVECLIM experiment whereas monthly temperature and δ^{18}Osw were used for the ECHAM5/MPI-OM experiment.

The surface density residuals anomalies (LGM - PI) are overall rather close to 0 except in the Nordic Seas region (north of 40°N in the Atlantic). For the following analyses we do not consider the North Indian Ocean for iLOVECLIM. Indeed, this region is affected by a well-known bias of this climate model due a shift of the African precipitation regions from the

456 west to the east of the continent, leading to much less saline waters than presently observed
457 (and unrealistically depleted $\delta^{18}Osw$) in the North Indian Ocean (Roche and Caley, 2013).
458 Higher residuals anomaly in Nordic Seas region could be associated with difficulty in
459 simulating the $\delta^{18}Osw$-salinity relation evolution related to ice-sheets and sea ice changes
460 and/or to foraminifera ecological changes between LGM and PI. We also observe in this
461 region larger surface density residuals anomalies (LGM – PI) with ECHAM5/MPI-OM than
462 with iLOVECLIM (Figure 5c and f). This can be explained by different simulated sea ice
463 coverage in ECHAM5/MPI-OM compared to iLOVECLIM. Indeed, the Nordic Seas is the
464 region with the largest difference between the two model simulations of modeled annual SST
465 below 0°C (https://doi.org/10.5194/egusphere-2025-2459-AC2). Temperature is used to
466 calculate the $\delta^{18}Oc$ signal, ocean density and to force the FAME module. Any temperature
467 difference in the Nordic Seas thus affects density reconstructions and hence the density
468 residuals (Figure 5c and f).

469

470 To further investigate in a more quantitative way if the use of the PI bayesian calibration to
471 predict LGM surface density introduces additional uncertainties, we compare probability
472 distributions of surface density residuals anomaly (LGM - PI) using violin and box plots to the
473 95% confidence interval (CI) of the PI bayesian calibration (Fig. 6). We consider each
474 foraminifera species separately. Global results indicate for the *G. ruber* and *T. sacculifer*
475 species that 1) the 5th to 95th percentile and interquartile range of the surface density
476 residuals anomaly is well inside the 95% CI of the PI bayesian calibration for both
477 ECHAM5/MPI-OM and iLOVECLIM experiment and 2) high probability and median values are
478 close to 0 (Fig. 6a and c). This is not the case for *G. bulloides*, *N. incompta*, and for *N.*
479 *pachyderma*.

480 When the Nordic Seas region is removed, results indicate that for all the foraminifera
481 species, the interquartile range of the surface density residuals anomaly is well inside the
482 95% CI of the PI bayesian calibration for both experiments (ECHAM5/MPI-OM and
483 iLOVECLIM). High probability and median values are closest to 0 (Fig. 6b and d). The 95% CI
484 of the PI bayesian calibration is closest to the 5th to 95th percentile range of the surface
485 density residuals anomaly.

486
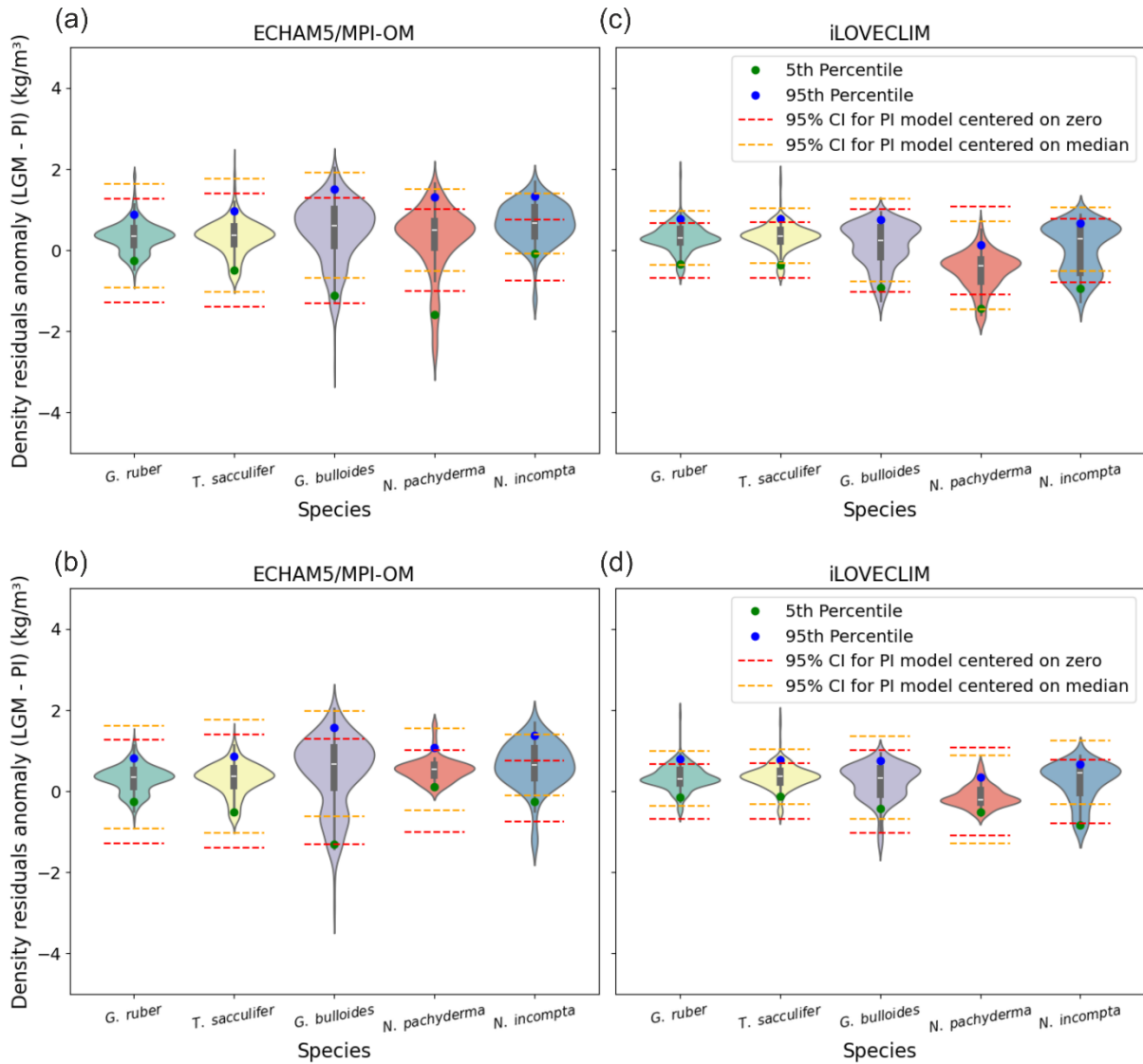
Figure 6: probability distributions of surface density residuals anomaly (LGM - PI) for ECHAM5/MPI-OM and iLOVECLIM, for global data (a and c), and without the Nordic Seas and northern North Atlantic (north of 40°N) (b and d). North Indian Ocean data for iLOVECLIM have been removed in both cases.

We conclude based on our tests that the use of a Bayesian calibration model (hierarchical design) to predict annual surface density during past periods (with the example here of the LGM climate) is valid globally within the explicitly estimated uncertainty in calibration model parameters, except for the Nordic Seas region.

3.2 Reconstruction of past ocean surface absolute density

To reconstruct past ocean surface absolute density based on foraminifera $\delta^{18}Oc$ values that have been corrected from the $\delta^{18}Osw$ ice effect, an additional correction is necessary. Indeed, it is necessary to account for mean ocean density changes related to ocean volume changes that affect mean ocean salinity. Without this additional correction, the ocean density reconstructed corresponds to density changes linked to hydrographic changes in SST and SSS.

503 To determine the mean ocean density change related to the change in ocean volume at LGM
504 we used model simulation results (ECHAM/MPI-OM and iLOVECLIM) and added or removed
505 1 psu salinity (Duplessy et al., 1991) in global salinity outputs. Note that adding 1 psu of
506 salinity at LGM in climate model simulations has only small effects on ocean dynamics.
507 Indeed, the effect is due to the small non-linearity in the sea-ice freezing, hence generating
508 small differences in regions of sea ice and deep water formation. We have tested it in new
509 simulations performed with the iLOVECLIM model and found the dynamical effect of a 1 psu
510 salinity change in the regions we are analyzing to be very small (not shown).

511 Both model simulations agree and yield a mean ocean salinity effect on density of 0.776 (σ =
512 0.02) for ECHAM/MPI-OM and 0.772 (σ = 0.02) for iLOVECLIM. We also performed a
513 calculation to estimate this effect based on observations (reference state based on present
514 day observations and LGM state based on Tierney et al., 2020 for SST and Duplessy et al.,
515 1991 for SSS) and found very consistent results (https://doi.org/10.5194/egusphere-2025-
516 2459-AC1).

517 Therefore, the additional correction that is necessary to reconstruct past ocean surface
518 absolute density at the LGM is estimated to be equal to + 0.77.

519 3.3 LGM annual surface density reconstruction

520 We applied the poly1_hier calibration model to the LGM and LH δ^{18}Oc foraminifera
521 database, excluding the Nordic Seas region, after subtraction of 1.0 ‰ from LGM δ^{18}Oc
522 values (Labeyrie et al. 1987; Schrag et al., 1996; Schrag et al., 2002; Adkins et al., 2002;
523 Duplessy et al., 2002) in order to reconstruct LGM and LH annual surface density. Absolute
524 LGM annual surface density was calculated by adding 0.77 to density changes linked to
525 hydrographic changes in SST and SSS. The benefit of our Bayesian model is the possibility to
526 propagate uncertainty from calibration into predictions of past climate conditions (Fig. 7).

527

528

529

530

531

532

533

534

535

536

537
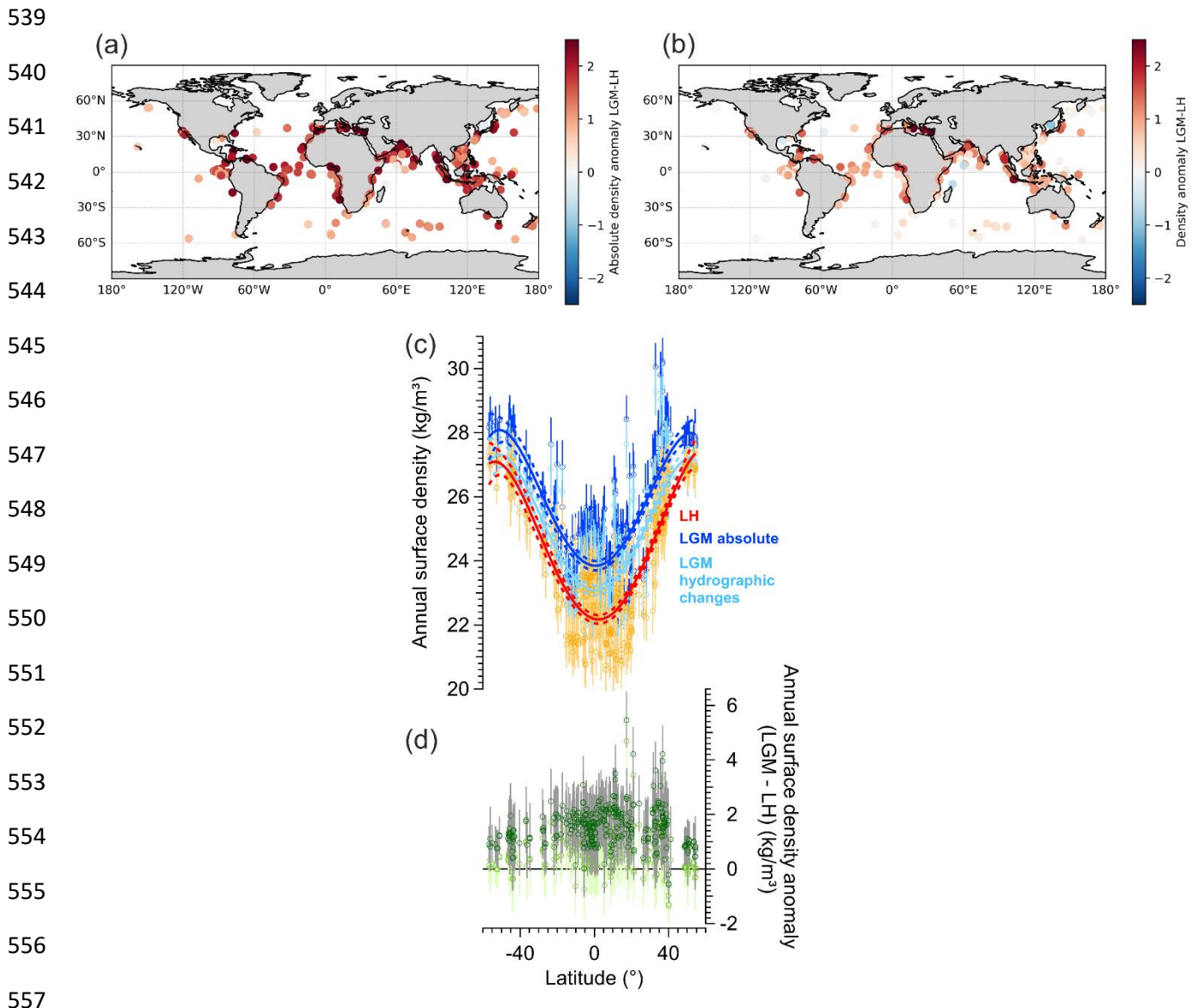
538

Figure 7: reconstructions of LGM and LH annual surface ocean density from foraminifera δ¹⁸Oc. (a) Spatial distribution of the LGM - LH absolute density anomaly. (b) Spatial distribution of the LGM - LH density changes due to hydrographic changes in SST and SSS. (c) Meridional gradient of reconstructed surface annual LGM density (absolute density in dark blue, density due to hydrographic changes in light blue) and comparison with LH reconstructions (red and orange colors). Error bars for each data point represent the 68 % C.I. A polynomial fit (5th degree) and associated 95% confidence bands are shown as solid resp. dashed lines. (d) Meridional gradient of reconstructed density anomaly (LGM - LH) for absolute density in dark green and density due to hydrographic changes in light green and associated 68 % C.I (grey lines).

Ocean surface density increases globally during the LGM in agreement with colder SST (MARGO, 2009; Tierney et al., 2020b) and increases global salinity (Duplessy et al., 1991; Adkins et al., 2002) (Fig. 7a). We also observe stronger LGM density value changes at low

572 latitudes compared to mid latitudes (Fig. 7b, c and d). This is probably the result of the LGM
573 cooling (MARGO, 2009; Tierney et al., 2020b) in combination with a reduction of the
574 intensity of low latitudes hydrological cycle (Kageyama et al., 2021), whereas higher latitudes
575 are already close to ocean density maximum. Further regional analyses of ocean surface
576 density and comparison with numerical climate models are presented in Barathieu et al. in
577 prep.

578

579 4. Conclusions

580 We developed three Bayesian regressions to model the relationship between the calcite
581 oxygen isotopic composition of planktonic foraminifera, $\delta^{18}Oc$, and annual mean surface
582 density, ρ. This allowed us to explicitly estimate the uncertainty in calibration model
583 parameters. We find that predictive performance of the model improves when we account
584 for inter-species specific differences. Before applying this model to past density
585 reconstructions, we used results of isotope enabled climate model simulations for PI and
586 LGM time periods to force the FAME module. We then investigated the additional
587 uncertainties that could be introduced by potential evolution of the $\delta^{18}Oc$-density
588 relationship with time. It could be caused by changes in the $\delta^{18}Osw$-salinity relationship or
589 by foraminifera ecology. We demonstrate that additional uncertainties are weak and that
590 our approach is valid (except for the Nordic Seas region), within propagated uncertainty
591 from calibration into predictions of past climate conditions.

592 By applying our Bayesian regression hierarchical model to LGM and LH $\delta^{18}Oc$ foraminifera
593 databases, we reconstructed LGM and LH annual surface density and found stronger LGM
594 density value changes at low latitudes compared to mid latitudes. The logical next step will
595 be to compare globally and in more detail (regional scale) our quantitative annual surface
596 density reconstruction with densities obtained by numerical climate model simulations
597 during the LGM. This will be used to evaluate these climate models in their ability to
598 simulate this parameter during this extreme climatic period (Barathieu et al., in prep). The
599 quantification of density together with the estimation of uncertainties could also be used for
600 data assimilation approaches, allowing local paleoclimate proxy information to be used to
601 infer global climate metrics (Tierney et al., 2020a).

602 We demonstrate that our approach is valid to quantitatively reconstruct annual surface
603 density during one of the coldest climates of the Quaternary period. We also demonstrate
604 this for the mid Holocene and last interglacial periods (Appendix B). Hence, our calibration
605 has great potential to be applied to other past periods and to reconstruct past temporal
606 evolution of ocean surface density downcore during the Quaternary. Under very extreme
607 climates outside the Quaternary (Appendix B) and in ocean basins characterized by anti-
608 estuary circulation, like the current Mediterranean Sea and Red Sea, our calibration could
609 provide density estimates with larger uncertainty, a point that requires further
610 investigations.

611 Finally, our calibration method to quantitatively reconstruct past ocean surface density is
612 stable with time. A combination with existing calibration methods to reconstruct past SST

613 could lead to a "time stable" method to quantitatively reconstruct past SSS over the
614 Quaternary, contrary to the use of the $\delta^{18}O_{sw}$-SSS approach. Before realized SSS
615 reconstructions, further investigations and calculation of uncertainties are necessary for this
616 potential new method. This is clearly a way forward as SSS is a crucial parameter that can
617 provide insights into hydrological cycle dynamics and its evolution.

618

619

620

621

622

623

624

625

626

627

628

629

630

631

632

633

634

635

636

637

638

639

640

641

Appendices

Appendix A. Detailed Prior Specifications

Below we provide the exact prior definitions and hyperparameter settings for each of the three Bayesian models. In the following, ρ denotes annual mean surface density, and δc represents $\delta^{18}Oc$. Let E[ρ] and var(ρ) be the sample mean and variance of ρ, respectively, and let var(δc) be the sample variance of δc.

1. **First-Degree Polynomial (Pooled)**

$$\rho \sim N(\mu, \sigma^2)$$
$$\mu = \beta_0 + \beta_1 \delta_c.$$

We chose weakly informative and data-adaptive priors, meaning they center around observed mean/variance but are broad enough to allow for uncertainty.

$$\beta_0 \sim N(E[\rho], 2.5\sqrt{var(\rho)}), \quad \beta_1 \sim N\left(0, 2.5\sqrt{\frac{var(\rho)}{var(\delta_c)}}\right), \quad \sigma \sim Exp(\sqrt{var(\rho)^{-1}}).$$

2. **Second-Degree Polynomial (Pooled)**

$$\rho \sim N(\mu, \sigma^2)$$
$$\mu = \beta_0 + \beta_1 \delta_c + \beta_2 \delta_c{}^2.$$

We set the priors to

$$\beta_i \sim N(0, 6.08^2)^{\square} \text{ for } i \in \{0, 1, 2\}, \quad \sigma \sim Exp(\sqrt{var(\rho)^{-1}}).$$

Here, the normal priors were chosen to ensure that 90 % of the prior mass for each β_i lies within [-10, 10].

3. **First-Degree Polynomial (Hierarchical)**

$$\rho \sim N(\mu_s, \sigma_s{}^2)$$
$$\mu_s = \beta_{s,0} + \beta_{s,1} \delta_c$$

where each species *s* has its own slope and intercept. These species-level parameters share hyperpriors:

Species-Level Parameters

$$\beta_{s,i} \sim N(\nu_i, \kappa_i{}^2), \quad i \in \{0, 1\}, \quad \sigma_s \sim Exp(\lambda_s).$$

Hyperpriors

682

684
$$\nu_0 \sim N(E[\rho], 10), \qquad \nu_1 \sim N(0, 10)$$

685
$$\kappa_0 \sim Exp(2.5\sqrt{var(\rho)}), \qquad \kappa_1 \sim Exp(2.5\sqrt{\frac{var(\rho)}{var(\delta_c)}}),$$

686
$$\lambda_s^{-2} \sim LogNormal(0, 1).$$

687

683

688

689
Appendix B. Application of our calibration to other past periods

690 Our study is focused on the LGM but it is interesting to examine if our results remain valid
691 for other climate periods. In this appendix, we present tests using isotope-enabled model
692 runs representing different past climate conditions in order to demonstrate that additional
693 uncertainties due to the evolution of the $\delta^{18}O_c$-density relationship with time are globally
694 small and that the new calibration has great potential to reconstruct the past temporal
695 evolution of ocean surface density over the Quaternary period.

696 In addition to the LGM time period investigated in our study, we tested the Mid Holocene
697 (MH) period and the last interglacial period (LIG) (Figs. B1 and B2). Results clearly indicate
698 a strong stability of foraminifera $\delta^{18}O_c$-density relations between MH, LIG and the PI, that is
699 a very weak influence of the changes in the $\delta^{18}O$/Salinity relation or foraminifer ecology (i.e.
700 habitat depth and growing season) on final density predictions (Figs. B1 and B2).

701

702

703

704

705

706

707

708

709

710

711

712

713

714
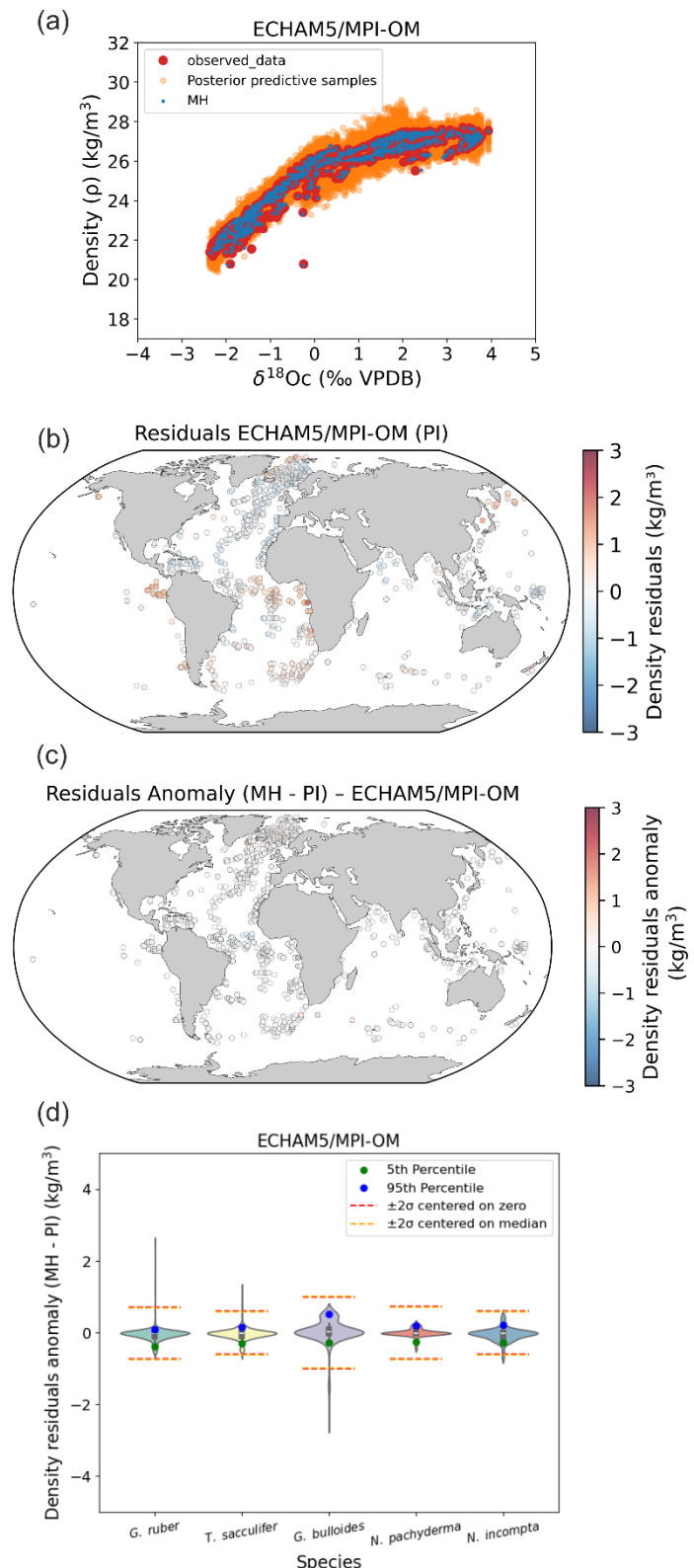
Fig. B1: Stability of foraminifera δ^{18}Oc-density relations between PI and the MH calculated with FAME and forced by global AWI-ESM-2.1-wiso (Shi et al., 2023) hydrographic data. (a) PI Bayesian regression models between foraminifera δ^{18}Oc and annual surface density. Posterior predictive samples and the MH δ^{18}Oc-density relation (MH) are visible. (b) Density residuals (predicted - observed) for the PI experiments. (c) Density residuals anomaly between MH and PI. (d) Probability distributions of surface density residuals anomaly (MH - PI) without Nordic Seas and northern North Atlantic (north of 40°N).
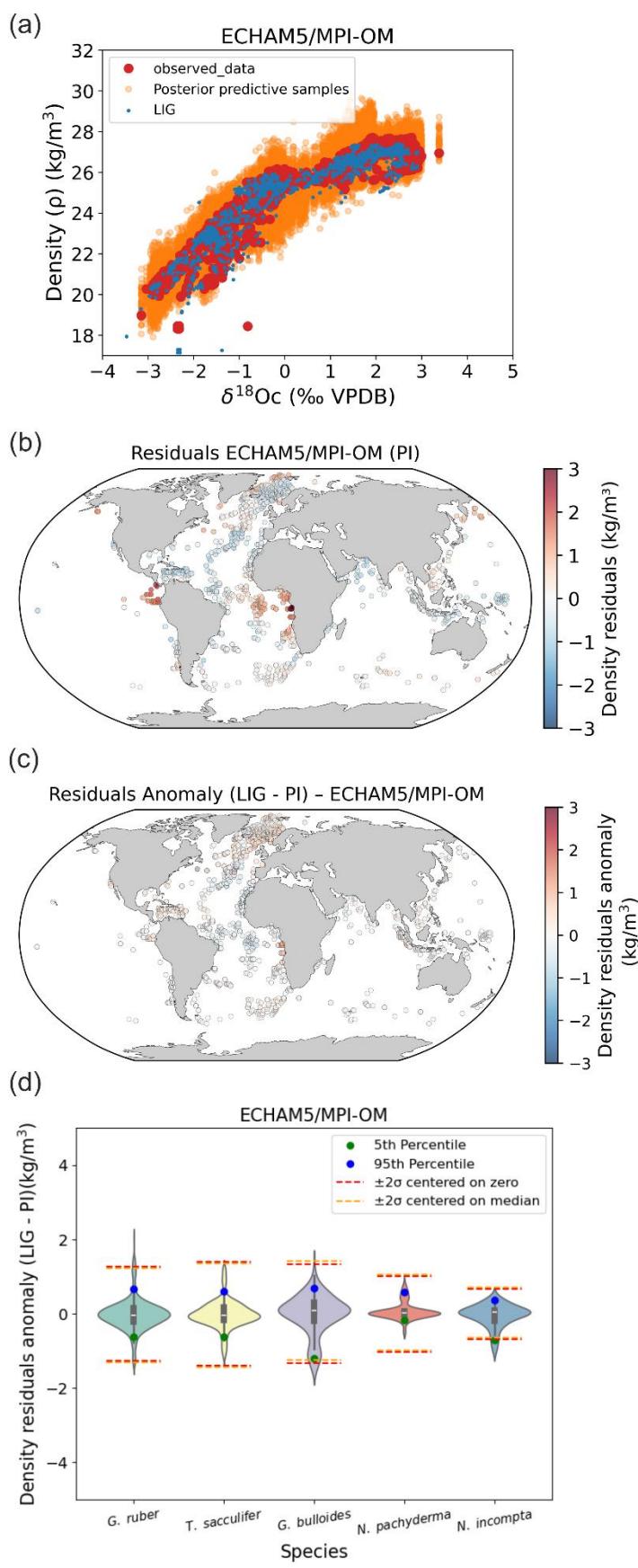
Fig. B2: Stability of foraminifera δ^{18}Oc-density relations between PI and the LIG calculated with FAME and forced by global ECHAM5/MPI-OM (Gierz et al., 2017) hydrographic data. (a) PI Bayesian regression models between foraminifera δ^{18}Oc and annual surface density. Posterior predictive samples and LIG δ^{18}Oc-density relations (LIG) are visible. (b) Density residuals (predicted - observed) for the PI experiments. (c) Density residuals anomaly between LIG and PI. (d) Probability distributions of surface density residuals anomaly (LIG - PI) without Nordic Seas and northern North Atlantic (north of 40°N).

Applying our calibration to past climates (and taking into account foraminifer ecological changes) provides density predictions that remain within the uncertainties of the calibration, as demonstrated for the LGM, MH and LIG time periods. These time periods correspond to extreme climate configurations over the Quaternary period as shown on Fig. B3, so the new calibration can be reliably applied to reconstruct the past temporal evolution of ocean surface density over the entire Quaternary (last 2.6 Ma).
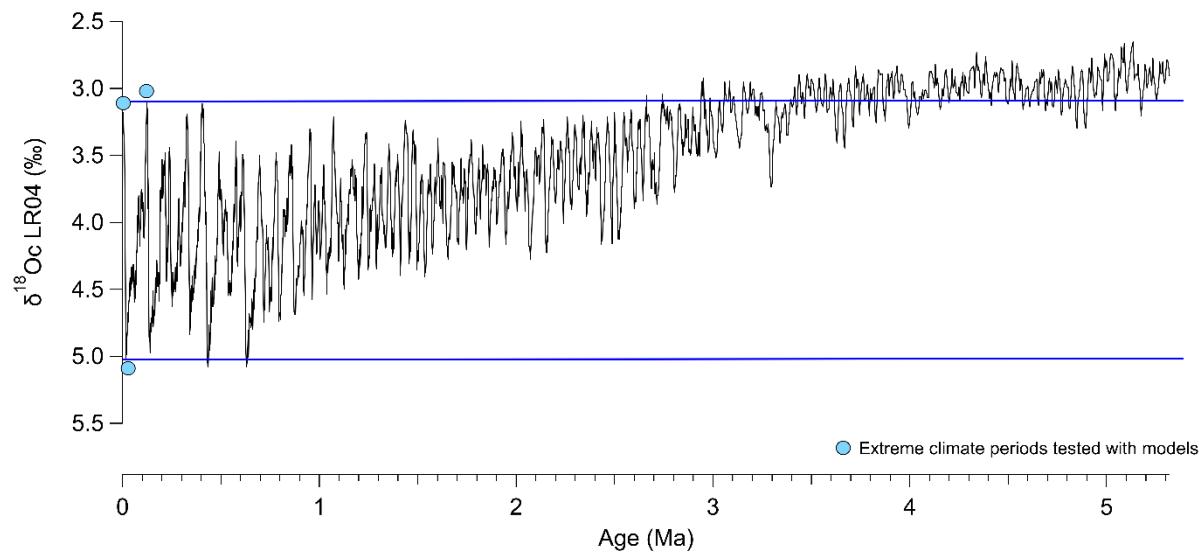
Fig. B3: δ^{18}O benthic foraminifera curve (LR04, Lisiecki and Raymo, 2005) as a proxy of ice volume and deep ocean temperature changes, used here to select extreme climatic periods (colder and more arid glacial periods versus warmer and more humid interglacial periods). Extreme climate periods tested with isotope-enabled model runs representing the mid-Holocene, LIG and LGM are represented by blue dots. Blue lines indicate the range of extreme climate conditions investigated with our climate simulations tests.

Nonetheless, under very extreme climates outside the Quaternary period (Fig. B3) and in ocean basins characterized by anti-estuary circulation, like the current Mediterranean Sea and Red Sea, our calibration could provide density estimates with larger uncertainty, a point that requires further investigations.

Code and data availability

The Python code for Bayesian calibration models is freely available at the following repository: https://github.com/nicrie/density_uncertainty. Core top data used for this analysis are from Malevich et al. 2019 and are available at https://agupubs.onlinelibrary.wiley.com/doi/10.1029/2019PA003576. LGM and LH δ^{18}Oc dataset are available at doi:10.5194/cp-10-1939-2014-supplement for Caley et al., 2014, at https://doi.org/10.1594/PANGAEA.894229 for Waelbroeck et al., 2014 and at https://doi.org/10.1594/PANGAEA.920596 for Tierney et al., 2020b. The additional LGM and LH δ^{18}Oc dataset is available at the following repository: https://github.com/nicrie/density_uncertainty.

Author contributions

TC and DR initially designed the study. TC developed the study. NR and TC developed the Bayesian calibration models. MW provided ECHAM5/MPI-OM model outputs. CW furnished the new δ^{18}Oc dataset. TC analysed the results with contribution and discussion of all co-authors. TC produced the figures and wrote the article with input from all co-authors.

Competing interests

The contact author has declared that none of the authors has any competing interests.

Acknowledgements

T.C. is supported by CNRS Terre & Univers. This study has been conducted using E.U. Copernicus Marine Service Information; https://doi.org/10.48670/moi-00051.

Financial support

This research was supported by the ANR HYDRATE project (grant no. ANR-21-CE01-0001) of the French Agence Nationale de la Recherche.

References

Adkins, J. F., McIntyre, K., and Schrag, D.: The salinity, temperature and δ^{18}O of the glacial deep ocean, Science 298, 1769–1773, 2002.

Bemis, B. E., Spero, H. J., Bijma, J., and Lea, D. W.: Reevaluation of the oxygen isotopic composition of planktonic foraminifera: experimental results and revised paleotemperature equations, Paleoceanography, 13, 150–160, 1998.

Bijma, J., Spero, H. J., and Lea, D. W.: Reassessing foraminiferal stable isotope geochemistry: Impact of the oceanic carbonate system (experimental results), in: Use of Proxies in Paleoceanography, edited by: Fischer, G. and Wefer, G., Springer Berlin Heidelberg, 489–512, 1999.

Billups, K. and Schrag, D. P.: Surface ocean density gradients during the Last Glacial Maximum. Paleoceanography, 15, 110–123, 2000.

846 Caley, T. and Roche, D. M.: δ^{18}O water isotope in the iLOVECLIM model (version 1.0) – Part 3:
847 A palaeo-perspective based on present-day data–model comparison for oxygen stable
848 isotopes in carbonates, Geosci. Model Dev., 6, 1505–1516, https://doi.org/10.5194/gmd-6-
849 1505-2013, 2013

850 Caley, T. and Roche, D. M.: Modeling water isotopologues during the last glacial: Implications
851 for quantitative paleosalinity reconstruction, Paleoceanography, 30, 739–750,
852 https://doi.org/10.1002/2014PA002720, 2015.

853 Caley, T., Roche, D. M., Waelbroeck, C., and Michel, E.: Oxygen stable isotopes during the
854 Last Glacial Maximum climate: perspectives from data-model (iLOVECLIM) comparison, Clim.
855 Past, 10, 1939–1955, doi:10.5194/cp-10-1939-2014, 2014.

856 Craig, H. and Gordon, L. I.: Deuterium and oxygen 18 variations in the ocean and the marine
857 atmosphere, in: Stable Isotopes in Oceanographic Studies and Paleotemperatures, edited by:
858 Tongiorgi, E., Lab. Geol. Nucl., Pisa, Italy, 9–130, 1965.

859 Droghei, R., Nardelli, B. B., and Santoleri, R.: Combining In Situ and Satellite Observations to
860 Retrieve Salinity and Density at the Ocean Surface, J. Atmos. Ocean. Tech., 33, 1211–1223,
861 https://doi.org/10.1175/JTECH-D-15-0194.1, 2016.

862 Droghei, R., Buongiorno Nardelli, B., and Santoleri, R.: A new global sea surface salinity and
863 density dataset from multivariate observations (1993–2016), Frontiers in Marine Science, 5,
864 https://doi.org/10.3389/fmars.2018.00084, 2018.

865 Duplessy, J. C., Lalou, C., and Vinot, A. C.: Differential Isotopic Fractionation in Benthic
866 Foraminifera and Paleotemperatures Reassessed, Science, 168, 250–251,
867 https://doi.org/10.1126/science.168.3928.250, 1970.

868 Duplessy, J. C., Labeyrie, L., Anne, Maitre, F., Duprat, J., and Sarnthein, M.: Surface salinity
869 reconstruction of the North Atlantic Ocean during the LGM, Oceanologica Acta, 14, 311–324,
870 1991.

871 Duplessy, J. C., Labeyrie, L., and Waelbroeck, C.: Constraints on the ocean oxygen isotopic
872 enrichment between the Last Glacial Maximum and the Holocene: Paleoceanographic
873 implications, Quaternary Sci. Rev., 21, 315–330, 2002.

874 Extier, T., Caley, T., and Roche, D. M.: Modelling water isotopologues (^{1}H^{2}H^{16}O, ^{1}H$_{2}$^{17}O) in the
875 coupled numerical climate model iLOVECLIM (version 1.1.5), Geosci. Model Dev., 17, 2117–
876 2139, https://doi.org/10.5194/gmd-17-2117-2024, 2024.

877 Gelman, A., Hwang, J., and Vehtari, A.: Understanding predictive information criteria for
878 Bayesian models. Stat. Comput., Springer US, 24, 997–1016, 2014.

879 Gibson, K. A., Thunell, R. C., Machain-Castillo, M. L., Fehrenbacher, J., Spero, H. J., Wejnert,
880 K., Nava-Fernández, X., and Tappa, E. J.: Evaluating controls on planktonic foraminiferal
881 geochemistry in the Eastern Tropical North Pacific, Earth Planet. Sc. Lett., 452, 90–103, 2016.

Gierz, P., Werner, M., and Lohmann, G.: Simulating climate and stable water isotopes during the Last Interglacial using a coupled climate-isotope model, J. Adv. Model. Earth Sy., 9, 2027–2045, https://doi.org/10.1002/2017MS001056, 2017.

Goosse, H., Brovkin, V., Fichefet, T., Haarsma, R., Huybrechts, P., Jongma, J., Mouchet, A., Selten, F., Barriat, P.-Y., Campin, J.-M., Deleersnijder, E., Driesschaert, E., Goelzer, H., Janssens, I., Loutre, M.-F., Morales Maqueda, M. A., Opsteegh, T., Mathieu, P.-P., Munhoven, G., Pettersson, E. J., Renssen, H., Roche, D. M., Schaeffer, M., Tartinville, B., Timmermann, A., and Weber, S. L.: Description of the Earth system model of intermediate complexity LOVECLIM version 1.2, Geosci. Model Dev., 3, 603–633, https://doi.org/10.5194/gmd-3-603-2010, 2010.

Hamilton, C. P., Spero, H. J., Bijma, J., and Lea, D. W.: Geochemical investigation of gametogenic calcite addition in the planktonic foraminifera Orbulina universa, Mar. Micropaleontol., 68, 256–267, 2008.

Jungclaus, J. H., Keenlyside, N., Botzet, M., Haak, H., Luo, J. J., Latif, M., Marotzke, J., Mikolajewicz, U., and Roeckner, E.: Ocean circulation and tropical variability in the coupled model ECHAM5/MPI-OM, J. Climate, 19, 3952–3972, 2006.

Kageyama, M., Harrison, S. P., Kapsch, M.-L., Lofverstrom, M., Lora, J. M., Mikolajewicz, U., Sherriff-Tadano, S., Vadsaria, T., Abe-Ouchi, A., Bouttes, N., Chandan, D., Gregoire, L. J., Ivanovic, R. F., Izumi, K., LeGrande, A. N., Lhardy, F., Lohmann, G., Morozova, P. A., Ohgaito, R., Paul, A., Peltier, W. R., Poulsen, C. J., Quiquet, A., Roche, D. M., Shi, X., Tierney, J. E., Valdes, P. J., Volodin, E., and Zhu, J.: The PMIP4 Last Glacial Maximum experiments: preliminary results and comparison with the PMIP3 simulations, Clim. Past, 17, 1065–1089, https://doi.org/10.5194/cp-17-1065-2021, 2021.

Kim, S.-T. and O'Neil, J. R.: Equilibrium and nonequilibrium oxygen isotope effects in synthetic carbonates, Geochim. Cosmochim. Acta, 61, 3461–3475, 1997.

Köhler, P. and Mulitza, S.: No detectable influence of the carbonate ion effect on changes in stable carbon isotope ratios (δ^{13}C) of shallow dwelling planktic foraminifera over the past 160 kyr, Clim. Past, 20, 991–1015, https://doi.org/10.5194/cp-20-991-2024, 2024.

Kruschke, J.: Doing Bayesian data analysis: A tutorial with R, JAGS, and Stan, Academic Press, Cambridge, Massachusetts, United States, 2014.

Labeyrie, L. D., Duplessy, J. C., and Blanc, P. L.: Variations in mode of formation and temperature of oceanic deep waters over the past 125,000 years, Nature, 327, 477–482, https://doi.org/10.1038/327477a0, 1987.

LeGrande, A. N., Lynch-Stieglitz, J., and Farmer, E. C.: Oxygen isotopic composition of Globorotalia truncatulinoides as a proxy for intermediate depth density, Paleoceanography, 19, PA4025, doi:10.1029/2004PA001045, 2004.

LeGrande, A. N. and Schmidt, G. A.: Water isotopologues as a quantitative paleosalinity proxy, Paleoceanography, 26, PA3225, https://doi.org/10.1029/2010pa002043, 2011.

920 Lisiecki, L. E. and Raymo, M. E.: A Pliocene-Pleistocene stack of 57 globally distributed
921 benthic δ^{18}O records, Paleoceanography, 20, PA1003, doi:10.1029/2004PA001071, 2005.

922 Locarnini, R., Mishonov, A., Baranova, O., Boyer, T., Zweng, M., Garcia, H., Reagan, J., Seidov,
923 D., Weathers, K., Paver, C., and Smolyar, I.: Temperature, in: World Ocean Atlas 2018, Vol. 1,
924 edited by: Mishonov, A., NOAA Atlas NESDIS 81, 2018.

925 Lombard, F., Labeyrie, L., Michel, E., Spero, H. J., and Lea, D. W.: Modelling the temperature
926 dependent growth rates of planktic foraminifera, Mar. Micropaleontol., 70, 1–7, 2009.

927 Lynch-Stieglitz, J., Curry, W. B., and Slowey, N.: A Geostrophic Transport Estimate for the
928 Florida Current from the Oxygen Isotope Composition of Benthic Foraminifera,
929 Paleoceanography, 14, 360–373, doi:10.1029/1999pa900001, 1999.

930 Lynch-Stieglitz, J., Adkins, J. F., Curry, W. B., Dokken, T., Hall, I. R., Herguera, J. C., Hirschi, J.
931 J.-M., Ivanova, E. V., Kissel, C., Marchal, O., Marchitto, T. M., McCave, I. N., Mc-Manus, J. F.,
932 Mulitza, S., Ninnemann, U., Peeters, F., Yu, E.-F., and Zahn, R.: Atlantic Meridional
933 Overturning Circulation During the Last Glacial Maximum, Science, 316, 66,
934 https://doi.org/10.1126/science.1137127, 2007.

935 Malevich, S. B., Vetter, L., and Tierney, J. E.: Global core top calibration of δ^{18}O in planktic
936 foraminifera to sea surface temperature, Paleoceanogr. Paleoclimatol., 34, 1292–1315,
937 2019.

938 MARGO Project Members: Constraints on the magnitude and patterns of ocean cooling at
939 the Last Glacial Maximum, Nat. Geosci., 2, 127–132, https://doi.org/10.1038/NGEO411,
940 2009.

941 McElreath, R.: Statistical rethinking: A bayesian course with examples in R and Stan,
942 Chapman and Hall/CRC, https://doi.org/10.1201/9781315372495, 2018.

943 Peeters, F. J. C., Brummer, G.-J. A., and Ganssen, G.: The effect of upwelling on the
944 distribution and stable isotope composition of Globigerina bulloides and Globigerinoides
945 ruber (planktic foraminifera) in modern surface waters of the NW Arabian Sea, Global
946 Planet. Change, 34(3–4), 269–291, 2002.

947 Ravelo, A. C. and Fairbanks, R. G.: Oxygen Isotopic Composition of Multiple Species of
948 Planktonic Foraminifera: Recorders of the Modern Photic Zone Temperature Gradient,
949 Paleoceanography, 7, 815–831, 1992.

950 Roche, D. M.: δ^{18}O water isotope in the iLOVECLIM model (version 1.0) – Part 1:
951 Implementation and verification, Geosci. Model Dev., 6, 1481–1491,
952 https://doi.org/10.5194/gmd-6-1481-2013, 2013.

953 Roche, D. M. and Caley, T.: δ^{18}O water isotope in the iLOVECLIM model (version 1.0) – Part 2:
954 Evaluation of model results against observed δ^{18}O in water samples, Geosci. Model Dev., 6,
955 1493–1504, https://doi.org/10.5194/gmd-6-1493-2013, 2013.

956 Roche, D. M., Waelbroeck, C., Metcalfe, B., and Caley, T.: FAME (v1.0): a simple module to
957 simulate the effect of planktonic foraminifer species-specific habitat on their oxygen isotopic

content, Geosci. Model Dev., 11, 3587–3603, https://doi.org/10.5194/gmd-11-3587-2018, 2018.

Rohling, E. J.: Paleosalinity: confidence limits and future applications, Mar. Geol., 163, 1–11, 2000.

Schiebel, R. and Hemleben, C.: Planktic Foraminifers in the Modern Ocean, Springer-Verlag, Berlin Heidelberg, 358 pp., 2017.

Schmidt, G. A.: Error analysis of paleosalinity calculations, Paleoceanography, 14, 422–429, 1999.

Schrag, D. P., DePaolo, D. J., and Richter, F. M.: Reconstructing past sea surface temperatures: Correcting for diagenesis of bulk marine carbonate, Geochim. Cosmochim. Acta, 59, 2265–2278, https://doi.org/10.1016/0016-7037(95)00105-9, 1995.

Schrag, D. P., Hampt, G., and Murray, D. W.: Pore fluid constraints on the temperature and oxygen isotopic composition of the glacial ocean, Science, 272, 1930–1932, 1996.

Schrag, D. P., Adkins, J. F., McIntyre, K., Alexander, J. L., Hodell, D. A., Charles, C. D., and McManus, J. F.: The oxygen isotopic composition of seawater during the Last Glacial Maximum. Quaternary Science Reviews, 21, 331–342, 2002.

Shackleton, N. J.: Attainment of isotopic equilibrium between ocean water and the benthonic foraminifera geuns Uvigerina: Isotopic changes in the ocean during the last glacial, Colloq. Int. du Cent. Natl. la Rech. Sci., 219, 203–210, 1974.

Shi, X., Cauquoin, A., Lohmann, G., Jonkers, L., Wang, Q., Yang, H., Sun, Y., and Werner, M.: Simulated stable water isotopes during the mid-Holocene and pre-industrial periods using AWI-ESM-2.1-wiso, Geosci. Model Dev., 16, 5153–5178, https://doi.org/10.5194/gmd-16-5153-2023, 2023.

Spero, H. J. and Lea, D. W.: Intraspecific stable isotope variability in the planktic foraminifera Globigerinoides sacculifer: Results from laboratory experiments, Mar. Micropaleontol., 22, 221–234, 1993.

Spero, H. J. and Lea, D. W.: Experimental determination of stable isotope variability in Globigerina bulloides: Implications for paleoceanographic reconstruction, Mar. Micropaleontol., 28, 231–246, doi:10.1016/0377-8398(96)00003-5, 1996.

Spero, H. J., Bijma, J., Lea, D. W., and Bemis, B. E.: Effect of seawater carbonate concentration on foraminiferal carbon and oxygen isotopes, Nature, 390, 497–500, 1997.

Tierney, J. E., Poulsen, C. J., Montañez, I. P., Bhattacharya, T., Feng, R., Ford, H. L., Hönisch, B., Inglis, G. N., Petersen, S. V., Sagoo, N., and Tabor, C. R.: Past climates inform our future, Science, 370, eaay3701, https://doi.org/10.1126/science.aay3701, 2020a.

Tierney, J. E., Zhu, J., King, J., Malevich, S. B., Hakim, G. J., and Poulsen, C. J.: Glacial cooling and climate sensitivity revisited, Nature, 584, 569–573, 2020b.

995 Urey, H. C.: The thermodynamic properties of isotopic substances, J. Chem. Soc., 562–581,
996 https://doi.org/10.1039/JR9470000562, 1947.

997 Vehtari, A., Gelman, A., and Gabry, J.: Practical Bayesian model evaluation using leave-one-
998 out cross-validation and WAIC, Stat. Comput., 27, 1413–1432,
999 https://doi.org/10.1007/s11222-016-9696-4, 2017.

1000 Vehtari, A., Gelman, A., Simpson, D., Carpenter, B., and Bürkner, P.-C.: Rank-Normalization,
1001 Folding, and Localization: An Improved $\hat{R}$ for Assessing Convergence of MCMC (with
1002 Discussion), Bayesian Anal., 16, 667–718, https://doi.org/10.1214/20-BA1221, 2021.

1003 Waelbroeck, C., Mulitza, S., Spero, H., Dokken, T., Kiefer, T., and Cortijo, E.: A global
1004 compilation of Late Holocene planktic foraminiferal $\delta^{18}O$: Relationship between surface
1005 water temperature and $\delta^{18}O$, Quaternary Sci. Rev. 24, 853–878, 2005.

1006 Waelbroeck, C., Kiefer, T., Dokken, T., Chen, M. T., Spero, H. J., Jung, S., Weinelt, M., Kucera,
1007 M., and Paul, A.: Constraints on surface seawater oxygen isotope change between the Last
1008 Glacial Maximum and the Late Holocene, Quaternary Sci. Rev., 105, 102–111,
1009 https://doi.org/10.1016/j.quascirev.2014.09.020, 2014.

1010 Werner, M., Haese, B., Xu, X., Zhang, X., Butzin, M., and Lohmann, G.: Glacial–interglacial
1011 changes in $H_2^{18}O$, HDO and deuterium excess – results from the fully coupled ECHAM5/MPI-
1012 OM Earth system model, Geosci. Model Dev., 9, 647–670, https://doi.org/10.5194/gmd-9-
1013 647-2016, 2016.

1014 Williams, D. F., Bé, A. W., and Fairbanks, R. G.: Seasonal oxygen isotopic variations in living
1015 planktonic foraminifera off Bermuda, Science, 206, 447–449, 1979.

1016 Zeebe, R. E.: An explanation of the effect of seawater carbonate concentration on
1017 foraminiferal oxygen isotopes, Geochim. Cosmochim. Acta, 63, 2001–2007,
1018 https://doi.org/10.1016/S0016-7037(99)00091-5, 1999.

1019 Zweng, M., Reagan, J., Seidov, D., Boyer, T., Locarnini, R., Garcia, H., Mishonov, A., Baranova,
1020 O., Weathers, K., Paver, C., and Smolyar, I.: Salinity, in: World Ocean Atlas 2018, Vol. 2,
1021 edited by: Mishonov, A., NOAA Atlas NESDIS 82, 2018.